Selective withdrawal of polymer solutions: computations

Diwen Zhou[1] and James J. Feng[1,2*]

[1]*Department of Chemical and Biological Engineering, University of British Columbia*
Vancouver, BC V6T 1Z3, Canada
[2]*Department of Mathematics, University of British Columbia, Vancouver, BC V6T 1Z2, Canada*

Abstract - This paper reports numerical simulations of selective withdrawal of Newtonian and polymeric liquids, and complements the experimental study reported in the accompanying paper [Zhou and Feng, Selective withdrawal of polymer solutions: experiments. J. Non-Newtonian Fluid Mech. submitted (2009)]. We use finite elements to solve the Navier-Stokes and constitutive equations in the liquid on an adaptively refined unstructured grid, with an Arbitrary Lagrangian Eulerian scheme to track its free surface. The rheology of the viscoelastic liquids are modeled by the Oldroyd-B and Giesekus equations, and the physical and geometric parameters are matched with those in the experiments. The computed interfacial deformation is in general agreement with the experimental observations. In particular, the critical condition for interfacial rupture is predicted to quantitative accuracy. Furthermore, we combine the numerical and experimental data to explore the potential of selective withdrawal as an extensional rheometer. For Newtonian fluids, the measured steady elongational viscosity is within 47% of the actual value, apparently with better accuracy than other methods applicable to low-viscosity liquids. For polymer solutions, an estimated maximum error of 300% compares favorably with prior measurements.

---

*Corresponding author. E-mail jfeng@chbe.ubc.ca

1   Introduction

Selective withdrawal refers to the drawing of one or both immiscible fluid components from stratified layers through a tube that is placed close to the interface (Fig. 1). Upon start of the suction, the interface dips in the center. If the suction rate is low, a steady state is achieved with a smooth interface. At higher flow rates in liquid-liquid systems, it is possible to draw out the top fluid as well [1]. Viewing this as an interesting process that couples interfacial deformation and bulk rheology, we have carried out concerted experimental and computational studies of selective withdrawal in an air-liquid system, with Newtonian and polymeric liquids. The experimental results, using silicone oils and dilute polymer solutions, are reported in the accompanying paper [2]. The main findings are: (*a*) the interfacial curvature is much greater for the polymer solutions than for a Newtonian one under comparable conditions, but the deformation is spatially more localized; (*b*) the surface of the polymer solutions ruptures at a critical flow rate, when a cusp forms directly above the suction tube from which a micron-sized air jet emanates toward the tube. No such critical behavior exists for viscous Newtonian liquids under air.

Thus, viscoelastic polymer solutions behave markedly differently from viscous Newtonian fluids in selective withdrawal. We have speculated in [2] that these differences arise from the viscoelastic stresses near the tip of the interface, where the polymer solution experiences elongational flow. We further speculated that this device may be used as an
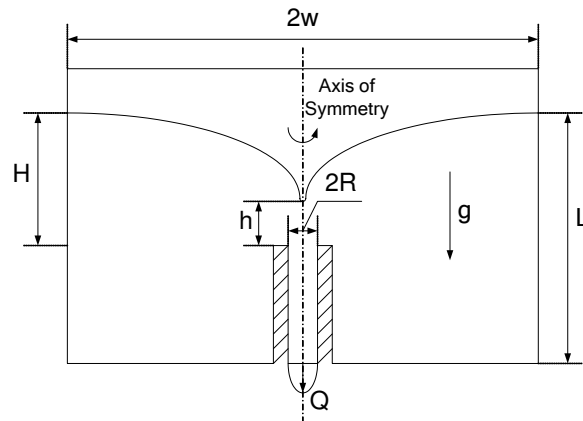

Figure 1: Schematic of selective withdrawal in an axisymmetric flow geometry. The computational domain is half of the meridian plane shown.

elongational rheometer if operated in the subcritical state. The force balance, between the polymer elongational stress and the capillary force, allows one to back out the former from the surface curvature and known interfacial tension. The present paper aims to substantiate these speculations by quantitative computation. In other words, we seek to confirm the polymer stress at the tip as the cause for the distinct behavior of polymer solutions, and to establish the feasibility of using selective withdrawal to measure the extensional viscosity of dilute polymer solutions.

To justify the impetus for testing new devices for measuring extensional viscosity, we briefly review the existing methods. The extensional viscosity is difficult to measure because it is very difficult to produce a purely extensional flow with a constant extensional rate in the laboratory [3]. There is a rich history of research on this subject, which can be appreciated through several comprehensive reviews [4–6]. Here, we will discuss three types of extensional rheometers of wide use today: filament stretching extensional rheometer (FiSER), capillary thinning extensional rheometer (CTER) and the opposed-nozzle rheometer.

In FiSER, a fluid bridge is formed between two end plates. When the end plates move apart exponentially, the central portion of the fluid experiences uniaxial elongation at an approximately constant rate, which can be determined from the thinning diameter of the fluid cylinder. This, together with the force on the end plate, allows one to calculate the extensional viscosity [7, 8]. The FiSER is attractive because of the direct control of the strain rate. But one limitation is that the liquid has to be sufficiently viscous as to form a smooth and stable filament when stretched. Typically this requires the zero-shear viscosity to be from 10 to 10^3 Pa·s. Another issue is the disturbance of the end plates. The flow is not elongational near the plates, and suffers from a de-adhesion instability at large stretching rates [9].

CTER is based on the capillary thinning of a liquid filament formed by abruptly separating two end plates that initially sandwiched a liquid bridge [10]. The diameter of the filament is recorded until breakup under the combined action of surface tension and extensional force. From the balance between these forces, one can back out the extensional viscosity [11–13]. A commercial version of CTER, known as CaBER, has been widely used in recent years [2, 14–16]. Compared with FiSER, CTER can handle fluids with relatively

low viscosity. But the extensional rate typically varies during the thinning process, and there is little control over it. Moreover, complicating factors such as inertia, gravity and axial curvature necessitate an ad hoc correction factor in order to produce a reasonable Trouton ratio for Newtonian fluids [11, 17]. Note that both FiSER and CTER report an *elongational stress growth viscosity* [18], which is the instantaneous elongational viscosity as a function of time or strain. Normally, it is difficult to reach steady-state stretching in terms of the stress growth. In fact, none of the existing devices can readily measure the steady-state elongational viscosity [4].

The opposed-nozzle device consists of two opposite nozzles aligned and submerged in the test fluid. When the fluid is drawn into both nozzles at the same rate, an extensional flow is created at the stagnation point between the nozzles [3, 19, 20]. The elongational rate is estimated from the flow rate, and the stress from the torque on one of the nozzles. Then an apparent elongational viscosity can be estimated. The advantage of the opposed-nozzle device is that it applies to low-viscosity fluids such as dilute polymer solutions. The disadvantage is that the flow field is rather complex. One has to use a nominal, rather than local, strain rate. The result also tends to be sensitive to inertia, nozzle size and separation, and eddies near the nozzles [21]. Finally, the fluid on different streamlines experiences different strains, with an average strain of order one [22]. It is unclear whether the measured elongational viscosity should be taken as the transient value corresponding to the average strain or the steady elongational viscosity at the nominal strain rate. The latter would be inaccurate since the polymers are unlikely to reach steady stretching at such a small strain. Even for Newtonian fluids, the opposed-nozzle device gives a Trouton ratio that deviates much from 3 [3, 20]; typical values range from 2–4 [19] to order 10 [23] and even 100 [24]. As a result, Dontula *et al.* [20] recommended using the device as an "indexer" rather than rheometer.

To sum up, the extensional viscosity of highly viscous liquids can be measured with relatively high accuracy using filament stretching. For low-viscosity fluids, on the other hand, an equally satisfactory method does not seem to be available. It is against this backdrop that we consider the potential of developing the selective withdrawal device into an extensional rheometer.

2   Governing equations and numerical methodology

Compared with the traditional fluid-dynamic simulation, the current problem presents two additional complications: non-Newtonian rheology in the liquid bulk, and the moving and deforming liquid surface. The rheology is modeled using Oldroyd-B and Giesekus equations. Together with the Navier-Stokes equations, these are discretized using a fully implicit time-stepping scheme. The interface is treated as a free surface, and is tracked using an Arbitrary Lagrangian-Eulerian (ALE) scheme. As these elements have been discussed in the literature, we give only a brief summary below.

2.1   Governing equations

The flow is governed by the Navier-Stokes equations:

$$\nabla \cdot \boldsymbol{v} \;=\; 0, \tag{1}$$

$$\rho \left(\frac{\partial \boldsymbol{v}}{\partial t} + \boldsymbol{v} \cdot \nabla \boldsymbol{v} \right) \;=\; -\nabla p + \rho \boldsymbol{g} + \nabla \cdot \boldsymbol{\tau}, \tag{2}$$

where $\boldsymbol{\tau}$ is the stress tensor. The polymer solutions used in the experiments are dilute [2]. Thus, we have used the Oldroyd-B and Giesekus models for their rheology. Writing $\boldsymbol{\tau} = \boldsymbol{\tau}_s + \boldsymbol{\tau}_p$, we have the solvent stress $\boldsymbol{\tau}_s = 2\eta_s \boldsymbol{D}$, with $\boldsymbol{D} = (\nabla \boldsymbol{v} + \nabla \boldsymbol{v}^{\mathrm{T}})/2$, and the polymer stress $\boldsymbol{\tau}_p$ obeying one of the following equations [18]:

$$\boldsymbol{\tau}_p + \lambda \boldsymbol{\tau}_{p(1)} \;=\; 2\eta_p \boldsymbol{D}, \quad \text{(Oldroyd-B model)} \tag{3}$$

$$\boldsymbol{\tau}_p + \lambda \boldsymbol{\tau}_{p(1)} + \alpha \frac{\lambda}{\eta_p} \boldsymbol{\tau}_p \cdot \boldsymbol{\tau}_p \;=\; 2\eta_p \boldsymbol{D}, \quad \text{(Giesekus model)} \tag{4}$$

where λ is the relaxation time, η_s and η_p are the solvent and polymer viscosities, and α is the mobility parameter. The subscript (1) denotes the upper convected time derivative. The Oldroyd-B model is relatively simple but captures the key features of viscoelasticity. However, as $De = \lambda \dot{\epsilon} \to 0.5$ in uniaxial elongation, it exhibits a well-known stress singularity. The Giesekus model has an additional quadratic term that produces shear-thinning and averts the singular stress blowup in elongational flows [18].

2.2 Interface tracking using Arbitrary Lagrangian-Eulerian scheme

Mathematically, boundary conditions need to be imposed on interfaces and free surfaces. But they move and deform according to the flow of the bulk fluids, and their location is not known a priori. Typically this requires an iterative procedure for coupling the bulk flow and the interfacial motion. We have adopted a sharp-interface formulation that deploys grid points directly on the interface, and tracks their motion as a result of the fluid flow and stresses. Our numerical code is based on an Arbitrary Lagrangian-Eulerian (ALE) scheme previously developed for simulating bubble growth in polymer foaming [25]. This scheme employs two coordinates: an Eulerian coordinate ($\boldsymbol{x}$) and a quasi-Lagrangian coordinate ($\boldsymbol{X}$) fixed on a moving mesh. On boundaries, including the free surface, the mesh velocity conforms to that of the boundary with an optional slip in the tangential direction. As the boundary nodes move, the mesh in the interior deforms smoothly according to a Laplace equation:

$$\nabla \cdot (k^e \nabla \boldsymbol{v}_m) = 0, \tag{5}$$

where k^e is the inverse of the local element volume [26, 27]. Then the mesh position is updated every time step according to $\boldsymbol{v}_m(\boldsymbol{x}, t) = \frac{\partial \boldsymbol{x}(\boldsymbol{X}, t)}{\partial t}$. As all the variables are defined on the moving grid, the Lagrangian derivatives must be computed as

$$\frac{d}{dt} = \frac{\partial}{\partial t} + \boldsymbol{v} \cdot \nabla = \frac{\delta}{\delta t} + (\boldsymbol{v} - \boldsymbol{v}_m) \cdot \nabla, \tag{6}$$

where $\frac{\delta}{\delta t}$ is the time derivatives defined on the moving grid point: $\frac{\delta}{\delta t} = \frac{\partial}{\partial t}|_{\boldsymbol{X} \text{fixed}}$.

2.3 Finite element method

The governing equations are solved in an axisymmetric geometry with an unstructured triangular mesh, which moves and deforms by the ALE scheme, and is adaptively refined near large interfacial curvature and coarsened near small curvature. As the result of this, each boundary segment subtends to roughly the same center angle. In time, the moving boundary tends to distort the mesh and compromise its quality. Using a quality criterion based on the aspect ratio of the elements, we re-mesh the computational domain when needed. A typical mesh is shown in Fig. 2.

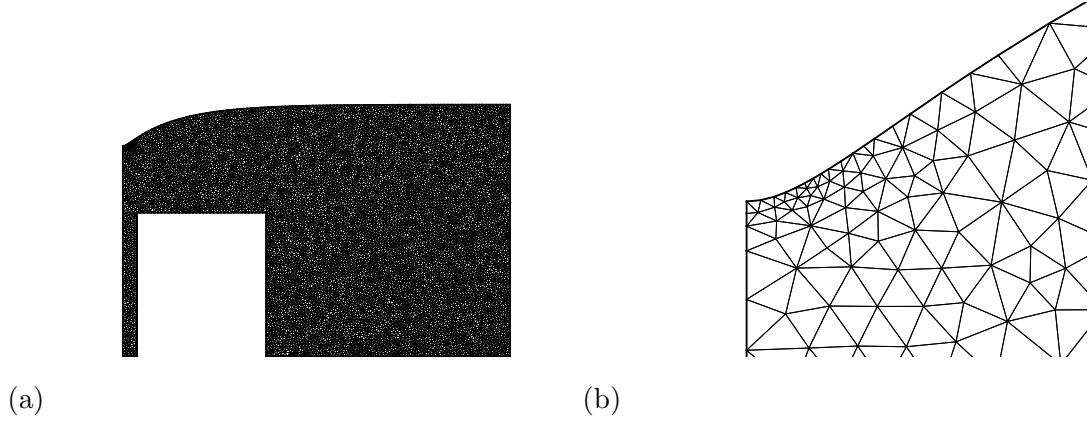(a)   (b)

Figure 2: A typical mesh used in our simulation. (a) The entire computational domain corresponding to half of the meridian plane of the axisymmetric geometry of Fig. 1. The left boundary is the axis of the suction tube, whose wall is the rectangular protrusion into the flow domain. (b) Magnified view of the mesh near the free surface. Note that the interface is marked by grid points, and the resolution is refined near the tip of the interface.

Using the standard Galerkin formalism to discretize the governing equation, we seek the weak solution $(\boldsymbol{v}, p, \boldsymbol{\tau})$ using the test functions $(\tilde{\boldsymbol{v}}, \tilde{p}, \tilde{\boldsymbol{\tau}})$, and in their weak form the governing equations become (taking the Oldroyd-B model for example):

$$\int_{\Omega} \left\{ \left[\rho \left(\frac{\delta \boldsymbol{v}}{\delta t} + (\boldsymbol{v} - \boldsymbol{v}_m) \cdot \nabla \boldsymbol{v} - \boldsymbol{g} \right) \right] \cdot \tilde{\boldsymbol{v}} + (-p\boldsymbol{I} + \boldsymbol{\tau}) \cdot \nabla \tilde{\boldsymbol{v}} \right\} r \, d\Omega - S = 0, \qquad (7)$$

$$\int_{\Omega} -(\nabla \cdot \boldsymbol{v}) \, \tilde{p} \, r \, d\Omega = 0, \qquad (8)$$

$$\int_{\Omega} \left\{ \boldsymbol{\tau}_p + \lambda \left[\frac{\delta \boldsymbol{\tau}_p}{\delta t} + (\boldsymbol{v} - \boldsymbol{v}_m) \cdot \nabla \boldsymbol{\tau}_p - \boldsymbol{\tau}_p \cdot (\nabla \boldsymbol{v}) - (\nabla \boldsymbol{v})^{\mathrm{T}} \cdot \boldsymbol{\tau}_p \right] \right. -$$
$$\left. \eta_p \left[\nabla \boldsymbol{v} + (\nabla \boldsymbol{v})^{\mathrm{T}} \right] \right\} \cdot \tilde{\boldsymbol{\tau}} r \, d\Omega = 0, \qquad (9)$$

where r is the radial coordinate in the axisymmetric geometry and S is the surface integral of the stress boundary condition:

$$S = \int_{\partial \Omega} \boldsymbol{n} \cdot (-p\boldsymbol{I} + \boldsymbol{\tau}) \cdot \tilde{\boldsymbol{v}} \, r \, dS = \int_{\partial \Omega_i} (-p_a + \kappa_s \sigma) \boldsymbol{n} \cdot \tilde{\boldsymbol{v}} \, r \, dS + \int_{\partial \Omega_\tau} \boldsymbol{n} \cdot (-p\boldsymbol{I} + \boldsymbol{\tau}) \cdot \tilde{\boldsymbol{v}} \, r \, dS, \quad (10)$$

where $\partial \Omega_i$ is the free surface subject to ambient pressure p_a, κ_s is the local curvature, σ is the surface tension, and $\partial \Omega_\tau$ is part of the boundary of the computational domain on which stress boundary condition are given. In addition, we also have the weak form of the Laplace equation for the mesh velocity:

$$\int_{\Omega} k^e \nabla \boldsymbol{v}_m \cdot \nabla \tilde{\boldsymbol{v}}_m \, d\Omega = 0. \qquad (11)$$

The simulation is advanced by second-order time stepping toward a steady state. At each time step, we iterate between solving the fluid flow and updating the surface position until convergence. In each iteration, the nonlinear algebraic equations resulting from Eqs. (7–11) are solved by Newton's method with delayed updating of the Jacobian. Within each Newton iteration, the linear system is solved by iterative methods such as the preconditioned generalized minimum residual (GMRES) scheme or the biconjugate gradient stabilized (BICG-STAB) algorithm. More details of the algorithm and validation with mesh refinement may be found in Yue *et al.* [25]. In our computations, the smallest grid size is typically around $0.1R$, R being the radius of the suction tube. This level of spatial resolution gives a discretization error below 1% in test problems.

As for most viscoelastic flow simulations, our computation is limited by the "high-Weissenberg number problem", i.e., the difficulty in achieving convergence at high Weissenberg numbers (or Deborah numbers in our nomenclature). This is typically because sharp gradients of the polymer stresses arise that cannot be adequately resolved numerically. In our computations, the steepest gradient appears at the lips of the suction tube, where the shear-rate is high and varies rapidly in space. To alleviate this problem, we introduced a rounding of the inner corner of the lip, with a radius of 1.1% of the tube radius. This allows us to improve the maximum Deborah number De from 4.1 to above 50. This is still below some of the experimental values of Zhou and Feng [2], and will pose some inconvenience in comparing the two.

2.4   Setup of the computational problem

In the computational domain shown in Fig. 1, the air-liquid interface is taken to be a free surface subject to a constant atmospheric pressure. Fluid enters from the bottom of the domain where zero-stress boundary condition is imposed. The side wall has no-slip boundary condition with vanishing velocity. On the axis of symmetry, of course, symmetry conditions are imposed. We have the following physical parameters: flow rate Q, interfacial tension σ, liquid viscosity η, density ρ and the gravitational acceleration g. The geometric parameters are the tube radius R, radius of the tank w, and the two heights L and H specifying the position of the free surface at the side wall relative to the tip of the tube and

the bottom of the tank. The main "dependent variables" are the position of the tip, given by h, and the surface curvature at the tip κ.

If the liquid is viscoelastic, the Giesekus model introduces three model parameters: the relaxation time λ, the mobility factor α, and the polymer viscosity η_p. Thus, in addition to the length ratios H/R, L/R and w/R, we have six dimensionless groups:

$$Ca = \frac{Q\eta}{\sigma R^2} \quad \text{(Capillary number)}, \tag{12}$$

$$Bo = \frac{\rho g R^2}{\sigma} \quad \text{(Bond number)}, \tag{13}$$

$$Re = \frac{\rho Q}{\eta R} \quad \text{(Reynolds number)}, \tag{14}$$

$$k = \frac{\eta_s}{\eta} \quad \text{(viscosity ratio)}, \tag{15}$$

$$De = \frac{\lambda Q}{R^3} \quad \text{(Deborah number)}, \tag{16}$$

$$\alpha \quad \text{(mobility factor)}, \tag{17}$$

where $\eta = \eta_p + \eta_s$. In the experiments, the flow Reynolds number is typically very small. In our simulation, therefore, we keep Re below 10^{-3} so that the flow is essentially inertialess. In addition, w and L will be large enough so as to avoid any influence from the side wall and the bottom of the domain. Thus, we have only one important length scale H/R and a total of six dimensionless parameters in our system. These may be varied, say, by changing Q, H, g, λ, η_s and α. Zhou and Feng [2] used an "elasticity number" $E = De/Ca$ to characterize the experimental fluids. This will also be used when comparing our simulations to experiments.

As the critical state is approached, the interface deforms into a cusp with the local curvature increasing without bound. This causes the local grid size to decrease toward zero, and the code diverges. Therefore we cannot simulate the transition from subcritical to supercritical state. In its stead, we employ a numerical criterion for determining the critical point in the simulations. With decreasing H at a fixed Q, the steady-state surface becomes more and more deformed, until at one point, no steady solution can be obtained and the code blows up. The average between the smallest H that gives a steady solution and the next H that does not is taken to be the critical H^* corresponding to the Q value. In the experiments, the tip curvature κ increases precipitously toward the critical condition. Thus, the fact that the numerically computable maximum κ depends on mesh resolution and is in some sense "arbitrary" does not appreciably affect the critical H^* value.
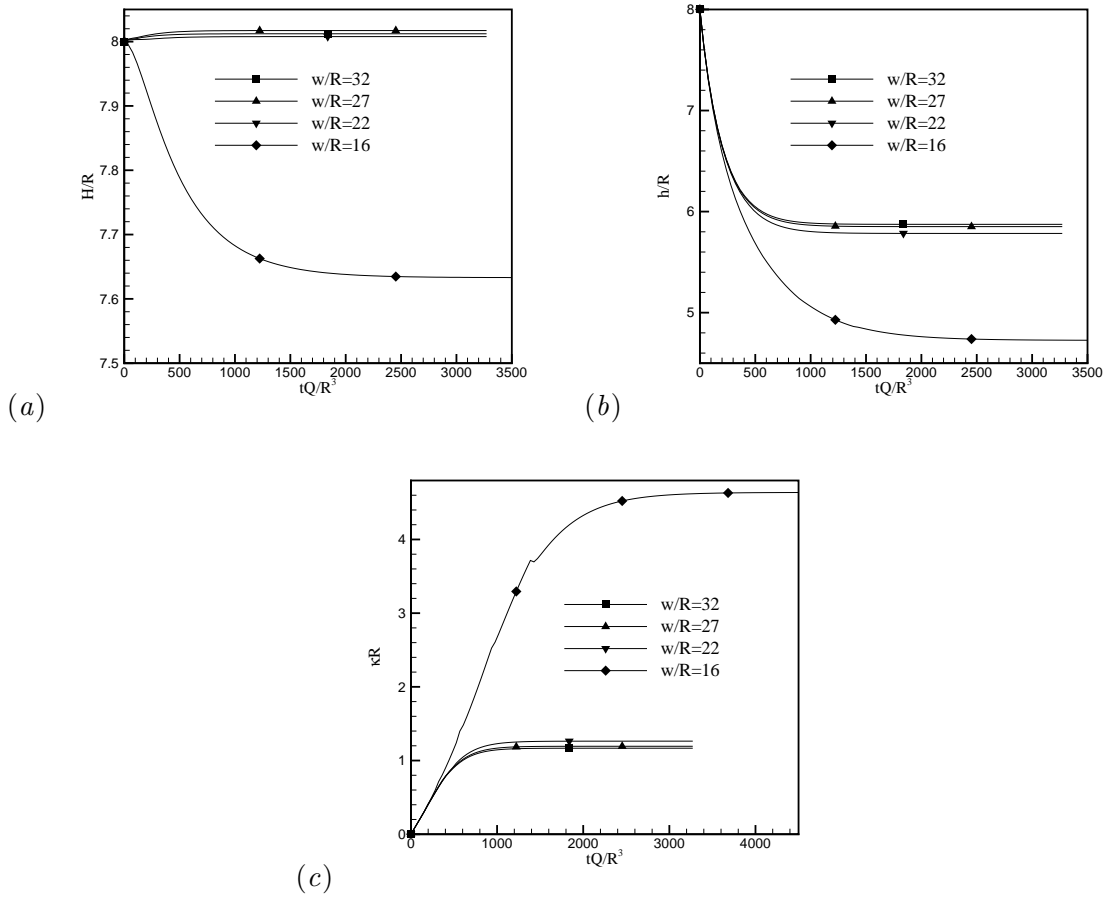
Figure 3: The side-wall effect in the simulation. (*a*) Variation of the water level at the side wall after the flow starts for four values of the tank radius w. (*b*) The position of the tip of the interface indicated by the vertical distance h from the tube. (*c*) Variation of the tip curvature. The wiggle on the curve for $w = 16R$ is a numerical artifact due to remeshing.

3 Newtonian results: benchmarking by experiments

The experiment of Courrech du Pont and Eggers [28] on air-oil selective withdrawal provides an ideal benchmark for our numerical algorithm. They used a tank of square cross-section, with the side $w = 27R$ wide enough so the results are unaffected by the side walls. To ensure negligible wall effects in our computations, we have tested four values of the tank radius w, and Fig. 3 plots the temporal variation of the water level at the side wall and the position and the curvature at the tip of the interface for each w value. When the width is large enough ($w \geq 27R$), H changes by only about 0.1% from the startup of flow till the
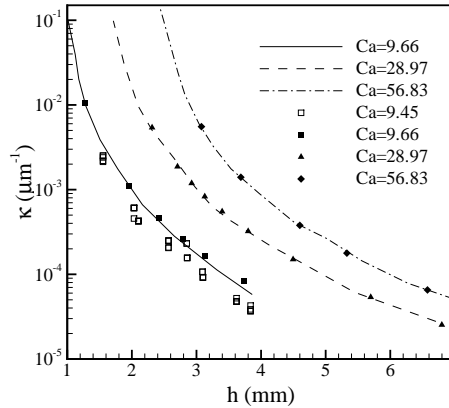
Figure 4: Comparison between our calculations (filled symbols), our experiment (open symbols) and the experiment of Courrech du Pont and Eggers [28] (lines). The capillary number Ca is varied through Q, and for each Ca different steady solutions are achieved by varying H. The Bond number is fixed at $Bo = 0.112$.

steady state. Moreover, Figs. 3(b) and (c) show that the side wall exerts little effect on the interface at the center for $w \geq 27R$. Thus $w = 27R$ is used for all subsequent computations.

Figure 4 compares our Newtonian simulations with the experimental data of Courrech du Pont and Eggers [28] for an air-oil system and with our own experiment described in Ref. [2]. All material parameters are matched between the three studies. Each point in Fig. 4 represents a steady state, and the data sets are generated by varying H for a fixed flow rate Q (or Ca). Increasing H leads to less deformation at the tip, with a smaller κ and larger h, because the interface is farther from the tube opening. There is nearly perfect agreement between our simulation and the experiments. Note that we tuned our computations to match $Ca = 9.66$ in [28]. But our experimental control is such that we reached a slightly lower $Ca = 9.45$. Accordingly the tip curvature is slightly below the two data sets at $Ca = 9.66$. In the parameter ranges tested, the numerical and experimental data seem to suggest a critical condition of $\kappa \to \infty$ at a finite h value. Because of finite numerical resolution, our computations cannot access $\kappa > 10^{-2}$ μm^{-1}. But additional evidence shows that a cusp ($\kappa \to \infty$) is unattainable for the low air-liquid viscosity ratio considered, and k remains finite [29]. This has been discussed at length in our experimental paper [2]. To sum up this section, the agreement with Newtonian experiments has validated our algorithm and code, and thus we are ready to turn to the viscoelastic problem.
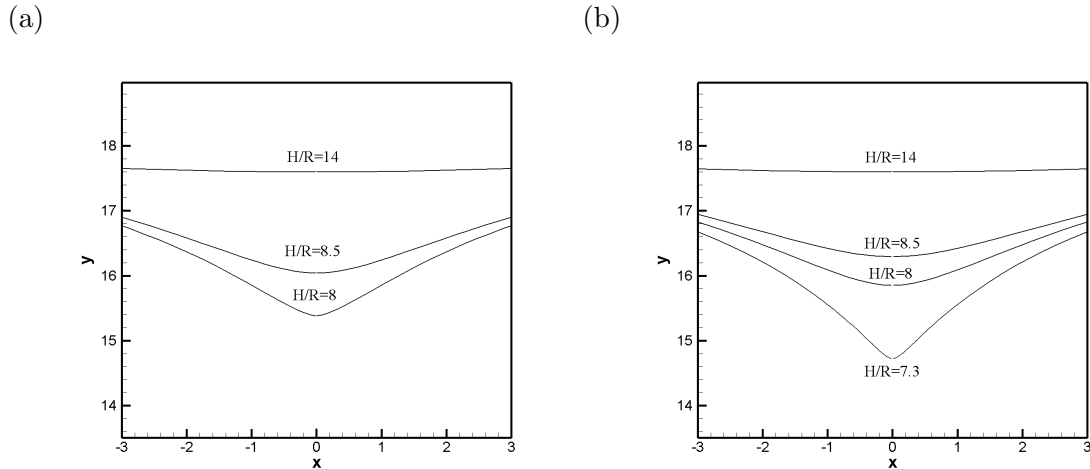
11

(a)

(b)

Figure 5: Steady-state interface profiles in the subcritical regime at several values of the liquid level H and a fixed $Ca = 28.97$. (a) Giesekus fluid with mobility factor $\alpha = 0.1$, viscosity ratio $k = 0.7$ and Deborah number $De = 12.29$. (b) Newtonian fluid.

4 Viscoelastic results

4.1 Interfacial deformation in subcritical regime

Figure 5(a) shows the steady-state free surface computed for the Giesekus fluid at a fixed $Ca = 28.97$ and different H values. As expected, the interface becomes more deformed with lowering H. The lowest curve for $H/R = 8$ is near the critical condition, even though the tip curvature appears rather mild. If H is lowered further, the steady-state κ increases sharply until the steady solution is lost. Numerically, the tip of the surface continues to extend and the computation diverges. For comparison, we plot in Fig. 5(b) the steady-state surfaces for a Newtonian fluid. The surface shape is qualitatively the same in both cases. However, for the same H values the surface is more deformed for the Giesekus fluid. Lacking a physical critical state, the Newtonian process can be computed to lower H with more deformed surfaces, until the tip curvature becomes too large to be resolved numerically. The lowest curve at $H/R = 7.3$ marks the limit of numerical convergence.

A more quantitative study of the viscoelastic effect is given in Fig. 6, which plots the tip position h and curvature κ as functions of the Deborah number De for Giesekus and Oldroyd-B fluids. For both models the results are qualitatively the same. As De increases,
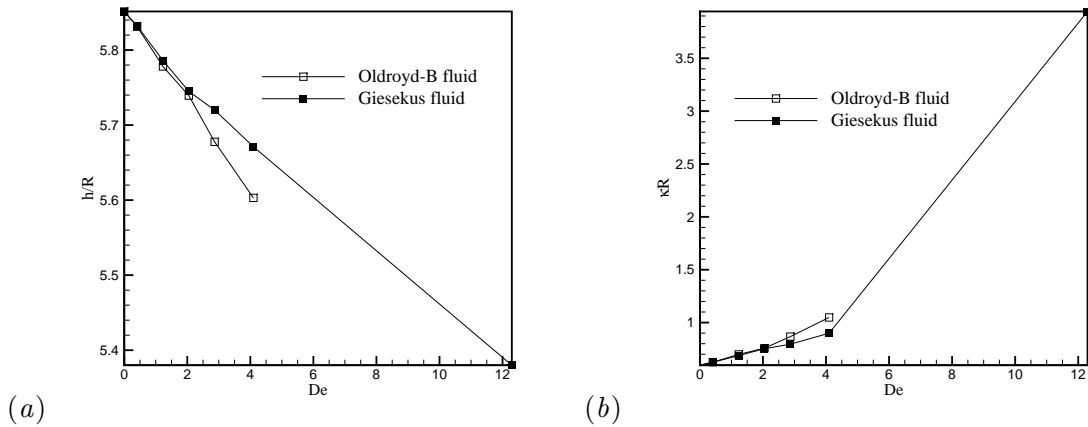
Figure 6: The effect of viscoelasticity, measured by the Deborah number De, on (a) the tip position h and (b) the tip curvature κ, for Oldroyd-B and Giesekus fluids. The following parameters are fixed: $Ca = 28.97$, $Bo = 0.112$ and $H/R = 8$. For the Giesekus fluid, $\alpha = 0.1$ and $k = 0.7$.

the tip moves progressively downward toward the suction tube; h decreases and the depth of depression $H - h$ increases. Meanwhile, the tip curvature κ increases monotonically. Both suggest increasing elongational force in the liquid that pulls the interface down. When De exceeds a critical value, the tip curvature seems to increase without bound and the simulation breaks down. As noted before, this is taken to be the critical state, which will be discussed at length in the next subsection. For the parameters in Fig. 6, the largest De we have computed is $De = 4.1$ for Oldroyd-B fluid and 12.29 for the Giesekus fluid. As is well known, the nonlinear term in the Giesekus model softens the strength of elastic stresses. Consequently, $H - h$ and κ are smaller than for the Oldroyd-B model at the same De. The critical state is also delayed to a higher De.

The greater surface deformation of viscoelastic liquids must stem from the polymer stress. To confirm this, we plot contours of the polymer stresses near the free surface for the Giesekus fluid at steady state (Fig. 7). The tensile stress $\tau_{zz} - \tau_{rr}$ dominates the other component, and is especially large in the region directly below the tip of the interface. That is where the flow is essentially uniaxial elongation. Furthermore, because of the vanishing velocity and long residence time there, the polymer experiences large strain and stretches to a much larger extent than elsewhere in the domain, thus producing the localized peak in the elongational stress. This reflects the well-known strain-hardening behavior of polymeric
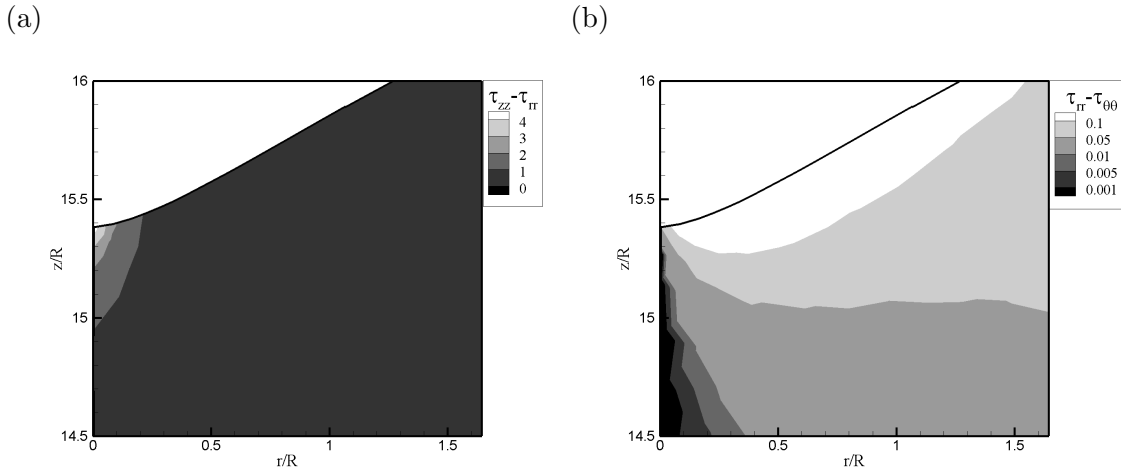
13

(a)

(b)

Figure 7: Contours of the normal-stress differences (a) $\tau_{zz} - \tau_{rr}$ and (b) $\tau_{rr} - \tau_{\theta\theta}$ near the steady-state surface for $H/R = 8$ in Fig. 5(a). $Ca = 28.97$, and the Giesekus fluid has $De = 12.29$, $k = 0.7$ and $\alpha = 0.1$.

liquids, where an elongational stress grows sharply with strain [18]. These considerations form the basis for the extensional rheometry to be discussed in Section 5.

Figure 8 compares a computed steady-state free surface for the Giesekus fluid with an experimentally measured free surface for a dilute polymer solution [2]. The Giesekus model parameters k and α are determined from the shear viscosity of the polymer solution and solvent. The experimental free surface is more deformed than the numerical prediction; the depression depth is underpredicted by about 10% and the tip curvature by 50%. Since the numerical parameters are matched to the experimental ones, the underprediction of surface deformation points to the Giesekus model not being able to reflect all aspects of the fluid's rheology.

4.2 Critical conditions

Computationally, the critical condition is approached by computing the steady solution for a series of decreasing H values, with the other parameters—De, Ca and rheological parameters—fixed. Thus, the critical condition is most conveniently marked by a threshold H^*. Unlike in the experiments, it is difficult to determine the critical h^* since near the critical point, h varies steeply with H. Taking the h value for the last steady solution for h^*
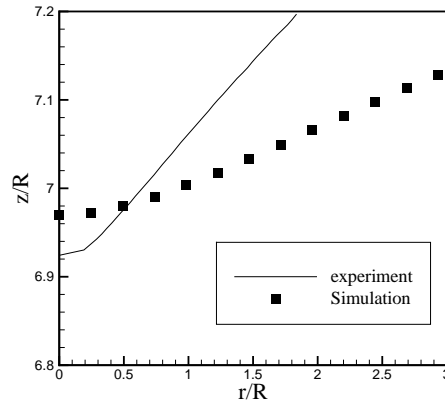
Figure 8: Comparison of the viscoelastic free surface between experiment and simulation. $Ca = 2.5$ and $H/R = 7.36$. The experiment uses the so-called "strongly elastic" fluid with elasticity number $E = De/Ca = 22.1$ and $De = 55.25$ [2]. The simulation is for a Giesekus fluid at $De = 55.25$, $k = 0.2$ and $\alpha = 0.2$.
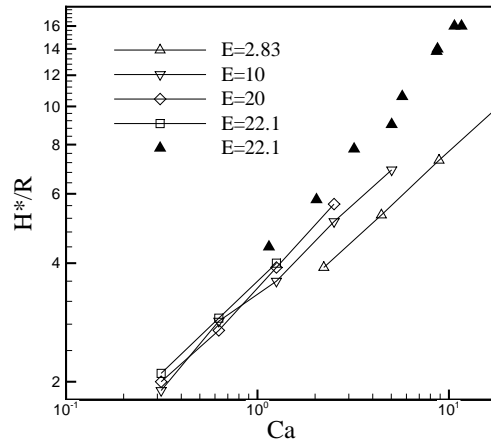

Figure 9: The critical liquid level H^* as a function of Ca at various E values for the Giesekus fluid. The lines with open symbols are numerical data and the filled symbols are experimental data from Ref. [2]. For the Giesekus model, $\alpha = 0.2$ and $k = 0.2$ match the shear rheology of the experimental fluid.

is likely to be a gross overestimation. Therefore, we will only discuss the critical condition in terms of H^*.

Figure 9 plots the critical liquid level H^* for a range of Ca and four values of the elasticity number $E = De/Ca$. Numerical results show that H^* increases with Ca and

E, in qualitative agreement with experimental observations (cf. Fig. 10 of Ref. [2]). As suggested in the experimental study, these trends reflect the fact that increasing either Ca or E leads to larger elastic stresses pulling down the interface. Thus the critical condition can be achieved for interfaces that are farther from the nozzle.

A quantitative comparison with experimental data is constrained by the maximum De computable in the simulations, which is about 55. The largest experimental De is over 200. As plotted in Fig. 9, the numerical data are limited to low Ca values for strongly elastic fluids with large E; for $E = 22.1$, the simulation covers a Ca range that barely overlaps the experimental range. Nevertheless, there seems to be good agreement between experimental and numerical data. This is reflected by the similar trend in the $H^*(Ca)$ dependence, which approximates straight lines in the log-log plot. Thus, both experimental and numerical data exhibit a power-law dependence on Ca. The slope of these lines increases with E consistently across all numerical and experimental data sets. For $E = 22.1$, the Giesekus model captures the slope of the experimental data accurately, but underpredicts the value of H^* by some 10%, consistent with the underprediction of surface deformation in Fig. 8.

Finally, we cannot simulate the supercritical state nor the hysteresis. In the experiment, the stability of the air jet depends on its small but non-zero mass and viscosity. In our computational setup, the air-liquid interface is treated as a free surface, with the air contributing no force on the interface aside from a constant ambient pressure. When we attempted to start the simulation with an initial condition having a thin air jet, the interface collapses in a short time and the code breaks down.

5 Measuring the elongational viscosity

To use selective withdrawal as an extensional rheometer, we need to satisfy three prerequisites: (a) to ensure that the flow near the tip is elongational; (b) to determine the elongational stress at the tip; (c) to determine the local strain rate at the tip. In the absence of direct velocity-field measurements, we will accomplish these objectives using data from numerical simulations. In the end, the validity of the scheme is established by comparing the measured elongational viscosity against benchmarks for Newtonian and polymeric liquids.
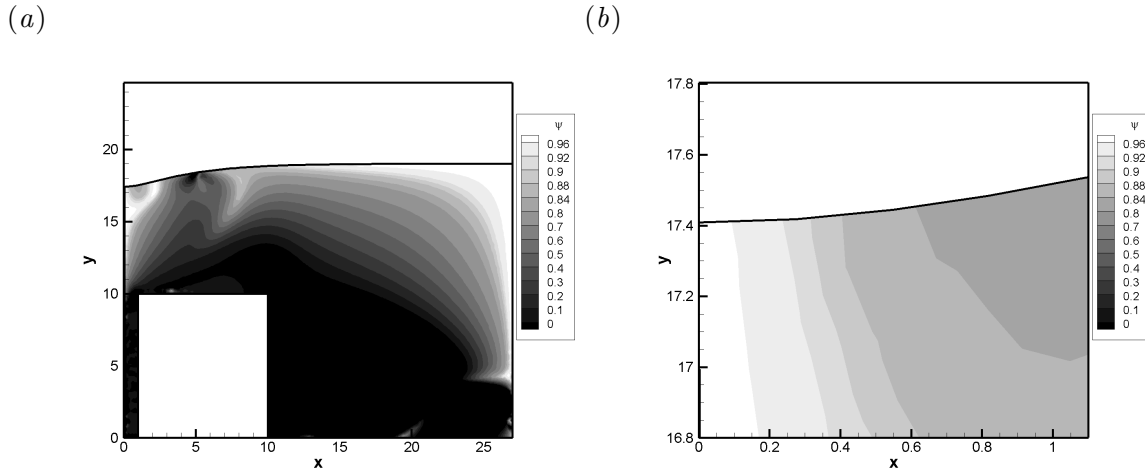
(a) (b)

Figure 10: Contours of the flow type parameter ψ in the computed flow field for a Giesekus fluid. Plot (b) shows details near the tip of the interface. In this case, $H/R = 9$, $Ca = 28.97$, $De = 12.29$, $k = 0.7$ and $\alpha = 0.1$.

5.1 Flow type

Following Singh and Leal [30], we use the *flow type parameter* to indicate how much of the deformation consists of extension and rotation:

$$\psi = \frac{\|\boldsymbol{D}\| - \|\boldsymbol{W}\|}{\|\boldsymbol{D}\| + \|\boldsymbol{W}\|}, \tag{18}$$

where $\boldsymbol{D} = (\nabla \boldsymbol{v} + \nabla \boldsymbol{v}^{\mathrm{T}})/2$ is the strain-rate tensor, and $\boldsymbol{W}$ is a modified vorticity tensor to maintain frame-indifference [30, 31]: $\boldsymbol{W} = \boldsymbol{\Omega} - \boldsymbol{O}$, where $\boldsymbol{\Omega} = (\nabla \boldsymbol{v} - \nabla \boldsymbol{v}^{\mathrm{T}})/2$ and $\boldsymbol{O}$ is the local rotation of the strain-rate tensor defined by

$$\frac{D\boldsymbol{e}_i}{Dt} = \boldsymbol{O} \cdot \boldsymbol{e}_i, \tag{19}$$

D/Dt being the material derivative and $\boldsymbol{e}_i$ the eigen-vectors of $\boldsymbol{D}$. Under this definition, $\psi = 1$ for purely extensional flow, 0 for simple shear and -1 for solid-body rotation.

Figures 10 depicts ψ contours in the computed flow fields for a Giesekus fluid. The magnified view shows that the flow is indeed very close to pure extension in the area below the tip of the interface. The same holds for Newtonian fluids. Thus our first prerequisite is satisfied.

17

5.2   Force balance

Now let us consider the force balance on the free surface at the tip. On the air side, the normal stress is the atmospheric pressure p_a. On the liquid side, we have pressure p_1 and a viscous or viscoelastic normal stress τ_{zz} in the vertical direction. On the interface there is the interfacial tension σ. Denoting the local curvature by κ, we modify the Laplace equation as such:

$$p_a = p_1 - \tau_{zz} + 2\sigma\kappa. \tag{20}$$

To determine p_1, we resort to the momentum equation in the horizontal (or radial in a cylindrical coordinate system) direction:

$$\rho\left(\frac{\partial v_r}{\partial t} + v_r\frac{\partial v_r}{\partial r} + \frac{v_\theta}{r}\frac{\partial v_r}{\partial \theta} - \frac{v_\theta^2}{r} + v_z\frac{\partial v_r}{\partial z}\right) = \left[\frac{1}{r}\frac{\partial(r\tau_{rr})}{\partial r} + \frac{\partial\tau_{\theta r}}{\partial \theta} + \frac{\partial\tau_{zr}}{\partial z} - \frac{\tau_{\theta\theta}}{r}\right] - \frac{\partial p}{\partial r}. \tag{21}$$

Because the flow is axisymmetric, $\tau_{\theta r} = 0$ and $\partial/\partial\theta = 0$. Neglecting the inertial terms for the moment, we have

$$\frac{\partial}{\partial r}(p - \tau_{rr}) = \frac{\tau_{rr} - \tau_{\theta\theta}}{r} + \frac{\partial\tau_{zr}}{\partial z}. \tag{22}$$

If the flow was homogeneous uniaxial elongation everywhere, τ_{rr} would equal $\tau_{\theta\theta}$ and τ_{zr} would vanish. Under this assumption we integrate from the tip ($r = 0$) radially outward to the wall ($r = w$):

$$p_1 - \tau_{rr}|_{r=0} = p_2 - \tau_{rr}|_{r=w}, \tag{23}$$

where p_2 is the pressure at the point on the wall that is level with the tip. Because the side wall is far from the suction tube (cf. Fig. 3), the local deformation rate is small. So we may set $\tau_{rr}|_{r=w} = 0$ and calculate p_2 from hydrostatics:

$$p_2 = p_a + \rho g(H - h). \tag{24}$$

From equations (20), (23) and (24), we get the first normal stress difference:

$$N_1 = \tau_{zz} - \tau_{rr} = 2\sigma\kappa + \rho g(H - h). \tag{25}$$

If the local strain rate $\dot{\epsilon}$ is known, the extensional viscosity can be obtained:

$$\bar{\eta} = \frac{N_1}{\dot{\epsilon}} = \frac{2\sigma\kappa + \rho g(H - h)}{\dot{\epsilon}}. \tag{26}$$

The determination of $\dot{\epsilon}$ will be discussed in the next subsection. Note that the derivation above applies equally to Newtonian and viscoelastic fluids.

This equation suffers from potential errors from three sources. The first is the neglect of inertial terms in Eq. (21). The second is setting $\tau_{rr} = \tau_{\theta\theta}$ and $\tau_{zr} = 0$ in Eq. (22) by assuming *homogeneous* uniaxial elongation. The third is the small-deformation-rate assumption along the side wall in Eqs. (23) and (24). The first and third turn out to be insignificant; the Reynolds number is low ($10^{-4} \sim 10^{-3}$), and the shear and normal stresses at the side wall are indeed negligible (about 0.1% of $\rho g(H - h)$). The second assumption is on less firm ground, and we will estimate the associated error in the following.

Integrating Eq. (22) without the assumption, we have

$$p_2 - (p_1 - \tau_{rr}) = \int_0^w \left(\frac{\tau_{rr} - \tau_{\theta\theta}}{r} + \frac{\partial \tau_{zr}}{\partial z} \right) dr, \tag{27}$$

which may be viewed as the error due to the shear component of the flow. Note that τ_{rr} is indeed equal to $\tau_{\theta\theta}$ on the axis of symmetry ($r = 0$) so that the integral does not diverge. Denoting this error by τ_{sh}, we have the following in place of Eq. (26):

$$\bar{\eta} = \frac{N_1}{\dot{\epsilon}} = \frac{2\sigma\kappa + \rho g(H - h) - \tau_{sh}}{\dot{\epsilon}}. \tag{28}$$

The magnitude of τ_{sh} should be dominated by the normal stress difference $\tau_{rr} - \tau_{\theta\theta}$ for small r. The τ_{zr} term should be insignificant because away from the centerline, where the flow contains considerable shear (cf. Fig. 10), the deformation rate dies out quickly. For a Newtonian fluid, $\tau_{rr} = 2\eta \frac{\partial v_r}{\partial r}$ and $\tau_{\theta\theta} = 2\eta \frac{v_r}{r}$. Toward the axis of symmetry, the $v_r(r)$ profile has to level to zero slope in a concave shape. Thus, we expect $\frac{\partial v_r}{\partial r} < \frac{v_r}{r} < 0$, $\tau_{rr} - \tau_{\theta\theta} < 0$ and $\tau_{sh} < 0$. Compared with Eq. (28), therefore, we expect Eq. (26) to underestimate the extensional viscosity.

This is borne out by numerical simulations for Newtonian liquids. After achieving a steady-state interfacial shape in the subcritical regime, the tip curvature κ, depression depth $H - h$ and the local strain-rate $\dot{\epsilon}$ are extracted from the numerical solution. Then the "measured" $\bar{\eta}$ from Eq. (26) is compared with the true elongational viscosity of the fluid $\eta_n = 3\eta$. Figure 11 illustrates the error of Eq. (26). Over the entire parameter space comprising Ca, Bo and H/R, the results confirm our argument that Eq. (26) *underestimates*
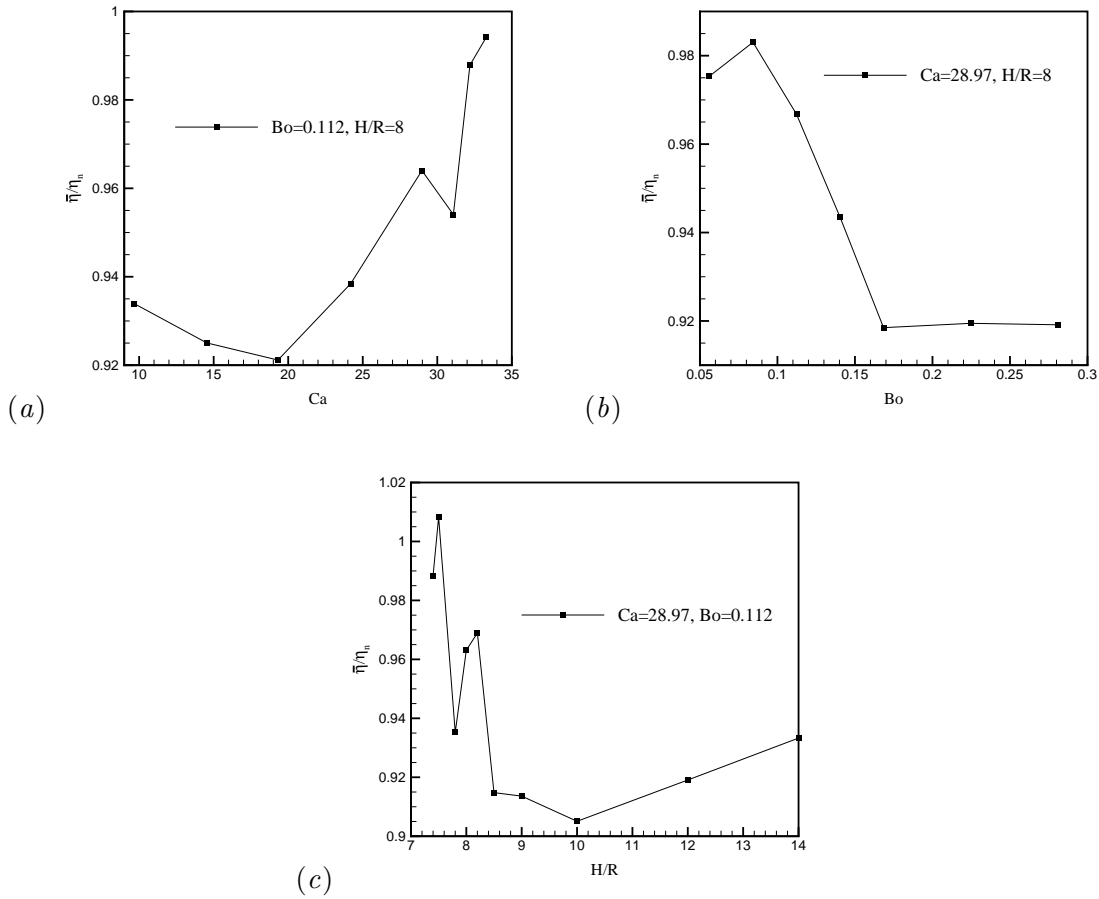
Figure 11: Testing the simplified Eq. (25) for estimating the extensional stress N_1 of Newtonian fluids. The "measured" $\bar{\eta}$, scaled by the known η_n, is plotted against Ca in (a), Bo in (b) and H/R in (c).

the elongational viscosity. But the magnitude of the error is within 10% for the parameter ranges covered. Considering that the opposed-nozzle rheometer easily suffers errors of 100% for Newtonian fluids [20], the results in Fig. 11 is very encouraging.

A similar exercise has been carried out for a Giesekus fluid (Fig. 12). In this comparison, η_G is the analytical extensional viscosity of the Giesekus model in steady-state elongation [18]. Now $\bar{\eta}$ is *overestimated* by Eq. (26); the neglected τ_{sh} turns out to be positive for the Giesekus fluid. Evidently this is because the shear away from the axis of symmetry tends to increase τ_{rr} relative to $\tau_{\theta\theta}$ (cf. Fig. 7b). This effect is particularly noticeable for smaller H/R values in Fig. 12(b); as the tip gets closer to the nozzle, the region of extensional
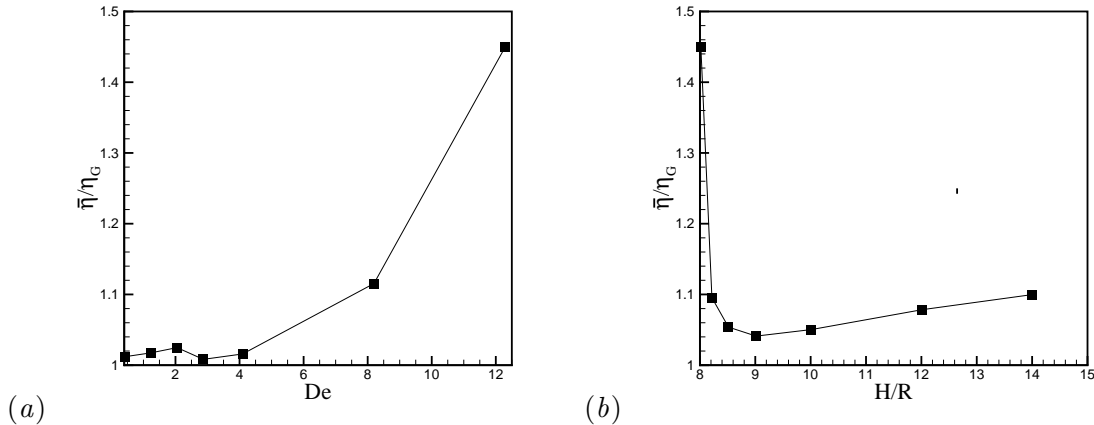
Figure 12: Testing the simplified Eq. (25) for estimating the extensional stress N_1 of Giesekus fluids. The "measured" $\bar{\eta}$, scaled by the known η_G, is plotted for (a) a range of De with $H/R = 8$, $\alpha = 0.1$ and $k = 0.7$; (b) a range of H/R with $De = 12.29$, $\alpha = 0.1$ and $k = 0.7$.

flow shrinks under the tip. For the conditions shown, $H/R = 8$ is approaching the critical condition. Nonetheless, the magnitude of the error is within 10% as long as the deformation is "not too strong", for a moderate $De < 6$ or $H/R > 8.2$. In summary, the simplified force balance of Eq. (25) can be used with acceptable accuracy to calculate the elongational stress N_1 from the surface force and hydrostatic pressure.

In writing the *steady-state* elongational viscosity in Eq. (26), we have tacitly assumed that the polymer has reached steady stretching under the local strain rate at the tip. This is true in principle since the polymer experiences infinite strain at the tip. In practice, however, we will measure the tip curvature using three neighboring points found from image processing [32]. Thus, Eqs. (25) and (26) involve a small but finite volume of liquid. To estimate the strain sustained by the polymer in this volume, we translate its physical size ($\sim 100\ \mu$m) onto the computational domain, and integrate the computed strain rate along streamlines passing through the volume. The minimum strain, on the outermost streamline, turns out to be about 7. Compared with prior filament-stretching experiments on dilute polymer solutions [7], this is sufficiently large for assuming steady-state stretching.

5.3 Local strain rate

In the absence of direct measurement of the extension rate $\dot{\epsilon}$ at the tip, we develop a correlation for $\dot{\epsilon}$ from the numerical data in terms of the material and control parameters of the system. Consider the Giesekus fluid given by Eq. (4). Dimensional analysis shows the strain rate at the tip to be a function of the six dimensionless groups:

$$\xi = \frac{\dot{\epsilon}R^3}{Q} = f\left(Ca, Bo, \frac{H}{R}, k, De, \alpha\right). \tag{29}$$

It would be very difficult to correlate ξ with all the parameters at once. Thus, we will first develop a correlation for Newtonian fluids, and then generalize it to the Giesekus fluid.

(*a*) *Newtonian correlation*

For a Newtonian system, Eq. (29) simplifies to:

$$\xi = f\left(Ca, Bo, \frac{H}{R}\right). \tag{30}$$

Similarly, the position of the tip h/R can also be expressed in the same three dimensionless groups. It turns out to be advantageous to rewrite Eq. (30) by using $\chi = (H - h)/R$ in place of H/R:

$$\xi = f\left(Ca, Bo, \chi\right). \tag{31}$$

As will be shown later, using χ facilitates generalization of the correlation to include viscoelastic effects.

Figure 13 plots ξ versus χ on a semi-log scale for a range of Ca and Bo values. All curves have the same gentle S shape, which we will represent linearly. The slope of the lines depends on Ca and Bo. After a curve-fitting exercise [32] we arrive at the following correlation:

$$\log \xi = A(Ca, Bo) + B(Ca, Bo)\chi, \tag{32}$$

with $A = (-2.01 + 0.41Bo)Ca^{0.15}$ and $B = (2.27 + 0.84 \log Bo)Ca^{-0.2}$. Of necessity, this form is a compromise between algebraic simplicity and fidelity. Its accuracy is examined in Fig. 14, where the y-axis is the ratio between the strain rate ξ_c given by Eq. (32) and the actual strain-rate ξ in the simulation at the same Bo and Ca values. Most of the data
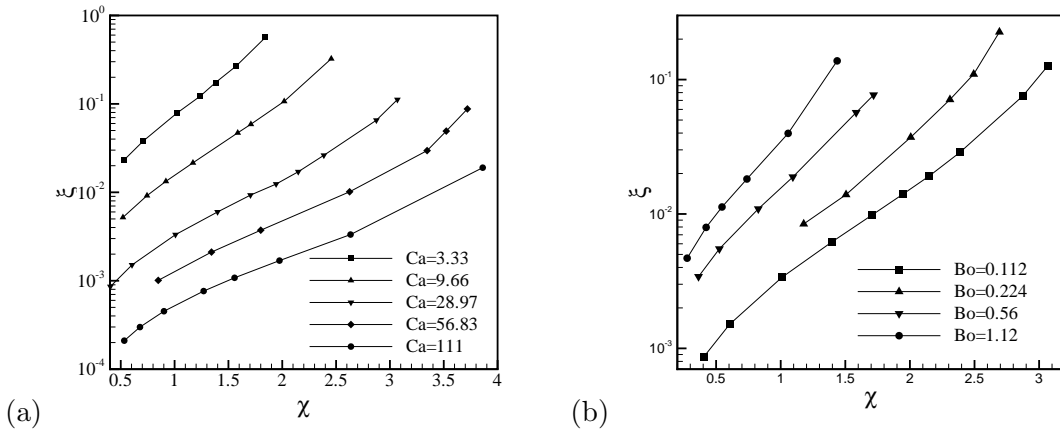
Figure 13: The dimensionless strain rate ξ at the tip as a function of χ for a Newtonian fluid for (a) a fixed $Bo = 0.112$ and a range of Ca values; and (b) a fixed $Ca = 28.97$ and a range of Bo values.
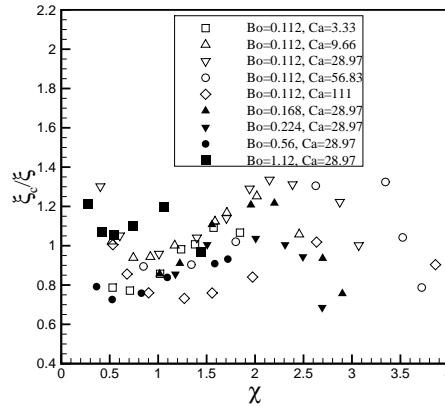

Figure 14: Accuracy of the Newtonian correlation Eq. (32) for the elongational rate.

points fall between 0.7 and 1.3, giving a margin of error of 30%. This is quite accurate in view of the range of error of prior rheometers.

(b) Viscoelastic correlation

As viscoelasticity enhances the tip curvature and depression depth (Fig. 6), so it also increases the strain rate at the tip. Under the conditions of Fig. 6, increasing De from 0 to above 12 causes $\dot{\epsilon}$ to increase by a factor of three for the Giesekus fluid. This dependence needs to be reflected through De, k and α in Eq. (29).
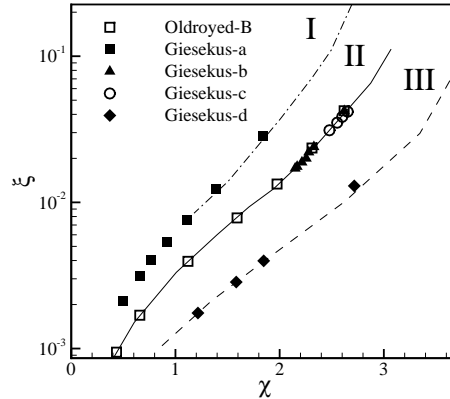
Figure 15: Collapse of the viscoelastic data for the tip strain rate onto the Newtonian data at the same Ca and Bo. Curve I represents Newtonian data for $Ca = 28.97$ and $Bo = 0.224$. Giesekus-a is for the Giesekus model with $De = 12.29$, $\alpha = 0.1$, $k = 0.7$, and χ varied via H. Curve II is Newtonian data at $Ca = 28.97$ and $Bo = 0.112$, onto which three viscoelastic data sets fall: Oldroyd-B with $De = 2.05$ and χ varied via H; Giesekus-b with $\alpha = 0.1$, $k = 0.7$ for a range of De; Giesekus-c with $De = 8.2$, $k = 0.7$ for a range of α. Curve III is Newtonian data at $Ca = 56.83$ and $Bo = 0.112$. The viscoelastic data Giesekus-d has $De = 24.12$, $\alpha = 0.1$, $k = 0.7$, and χ varied via H.

For reasons that we cannot yet explain, all the viscoelastic data collapse onto the Newtonian data if plotted as ξ versus $\chi = (H - h)/R$ instead of H/R. We have so far computed Giesekus and Oldroyd-B models at several Ca and Bo values with the following range of rheological parameters: $0.41 < De < 12.3$ and $0.01 < \alpha < 0.1$. Figure 15 depicts the collapse. Clearly, the polymer elongational stress tends to increase the depression depth χ and the tip extensional rate ξ simultaneously. Meanwhile, increasing the viscous stress (or Ca) will have similar effects. Our result shows that the same relationship between χ and ξ holds regardless of the agent—viscous or viscoelastic—that has prompted their change.

Figure 16 examines the error of the correlation Eq. (32) against numerical simulations for viscoelastic fluids. As in Fig. 14, The y-axis is the ratio ξ_c/ξ, with ξ being the actual local strain rate from simulations and ξ_c is that given by the correlation at the same Ca, Bo and χ values. In all the cases, the value of ξ_c/ξ falls between 0.75 and 1.4. Therefore, Eq. (32) applies to viscoelastic fluids with adequate accuracy.

This has two important implications: (a) The role of the polymer tensile stress in increasing the local $\dot{\epsilon}$ is fully accounted for by how much the tip is drawn toward the orifice.
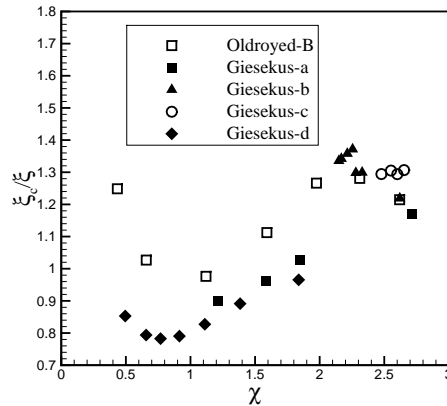
24

Figure 16: Accuracy of the correlation for elongational rate (Eq. 32) for viscoelastic fluids. The Oldroyd-B and Giesekus data sets are the same as in Fig. 15.

(*b*) For the extensional rheometer, the formulas of Eq. (26) and Eq. (32) can be used to obtain the elongational viscosity of Newtonian as well as viscoelastic liquids. The latter observation is quite convenient, but its accuracy remains to be confirmed by comparison with experimental data.

5.4 Benchmarking

To use a selective withdrawal device to measure the elongational viscosity of a liquid in the laboratory, one measures the interfacial position (in terms of h and H) and the tip curvature κ for a steady-state surface, uses Eq. (32) to estimate the local strain rate $\dot{\epsilon}$, and Eq. (26) to obtain the elongational viscosity $\bar{\eta}$. This scheme can be benchmarked by performing the selective withdrawal experiment on a liquid with known elongational viscosity. For Newtonian fluids, this is straightforward as the Trouton ratio is known to be three. For polymeric liquids, it is difficult to find a definitive benchmark.

(*a*) *Newtonian fluids*

Zhou and Feng [2] used silicone oil for selective withdrawal experiments, which has a density of 760 kg/m^3 and shear viscosity of 12.9 Pa·s at room temperature. The interfacial tension, measured using the ring method, is 21.3 mN/m. Figure 17 plots the Trouton ratio of the silicone oil measured by selective withdrawal, over a range of the strain rate $\dot{\epsilon}$ at
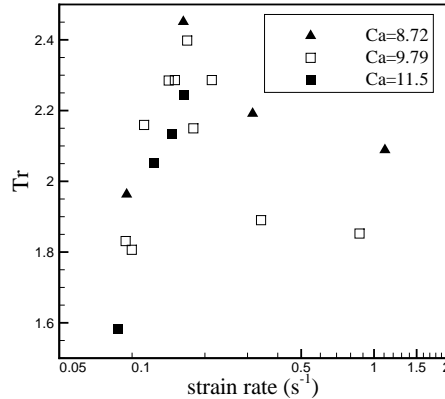
Figure 17: The Trouton ratio of silicone oil measured by selective withdrawal.

three capillary numbers. At each fixed flow rate or Ca, $\dot{\epsilon}$ is changed by varying the surface location H.

The three data sets for different Ca values more or less coincide. Thus, the measurement is intrinsic to the fluid rather than affected by the flow situations. This lends confidence to the validity of the scheme. However, the Trouton ratio ranges from 1.6 to 2.4, indicating that the scheme underestimates the elongational viscosity by up to 47%. Since the elongational stress is underestimated by 10% (Fig. 11), and the strain rate is subject to 30% of errors (Fig. 14), perhaps the magnitude of the error here is not surprising. But it is not clear why none of the data points exceeds $T_r = 3$. This level of accuracy compares favorably with existing devices. For instance, the opposed-nozzle device produced Trouton ratios between 4.5 and 7 for Newtonian fluids in Ref. [20].

(b) Polymer solutions

Benchmarking the selective withdrawal process for polymeric liquids is a subtler affair since there are no reliable methods to measure $\bar{\eta}$, especially for low-viscosity Boger liquids and at relatively low strain rates [4,33]. Indeed, this was largely the motivation for examining the selective withdrawal process for this purpose. Possible candidates are the filament stretching elongational rheometer (FiSER), the capillary breakup elongational rheometer (CaBER) and the opposed-nozzle device. As explained earlier, selective withdrawal probes

polymers that undergo large strains at the tip; thus, the measured $\bar{\eta}$ corresponds to steady stretching. In contrast, FiSER and CaBER provides a transient elongational stress growth viscosity $\bar{\eta}^+$ as a function of time or strain [18]. Steady-state stretching is seldom attained. In the opposed-nozzle device, the average strain across streamlines that enter the nozzles is roughly unity [22], probably insufficient for steady-state stretching.

Under these constraints, we adopt a two-pronged approach. On the one hand, we fit the shear rheology of our polymer solutions [2] into a Giesekus model. Then the *theoretical* elongational viscosity $\bar{\eta}$ is calculated, similar to that depicted in Fig. 7.3-8 of Bird *et al.* [18], and is used to benchmark the $\bar{\eta}$ measured from selective withdrawal. On the other hand, we take $\bar{\eta}^+$ data measured by James and Ouchi [34] using FiSER for a rough comparison with our measurements.

Our experiments have used polyisobutene solutions in polybutene and heptane [2]. For the benchmarking to be discussed here, we will only use data for the more concentrated "strongly elastic fluid". Its relaxation time has been measured by CaBER to be $\lambda = 8.5$ s. The shear rheology has been measured on a Bohlin rotational rheometer, and the polymer and solvent viscosities, as appear in the Giesekus model, are $\eta_p = 16.75$ Pa·s, $\eta_s = 4.25$ Pa·s at 21°C, with a viscosity ratio $k = 0.2$. The mobility factor α is obtained from fitting the shear-thinning at larger shear rates: $\alpha = 0.2$.

Figure 18 compares $\bar{\eta}$ measured by selective withdrawal with the theoretical value of the Giesekus model. First, as in the Newtonian benchmark, the data sets for three Ca values roughly collapse onto one master curve. Second, the measured $\bar{\eta}$ values are within a reasonable range of the theoretical prediction. The data fall below the Giesekus curve for $\dot{\epsilon} < 0.1$ s^{-1}, and overshoot it for higher strain rates. Over the entire range, the difference between the two is within a factor of 3. If the Giesekus benchmark is taken to be the true elongational viscosity of the fluid, this margin of error is quite acceptable in view of the poor accuracy of existing methods [4, 20, 33]. For example, the opposed-nozzle device yielded an $\bar{\eta}$ more than one order of magnitude smaller than that measured by fiber spinning [4, 35]. Schweizer *et al.* [35] attributed this to the spatial inhomogeneity of the flow field, where polymers on streamlines away from the stagnation point experiences short residence time and modest stretching. Contraction flows also produced an order of magnitude of
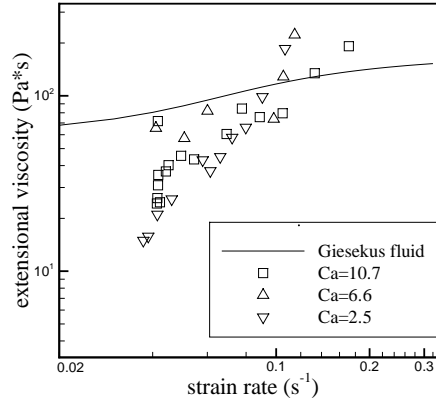
Figure 18: Comparison of the elongational viscosity measured by selective withdrawal with the theoretical value of the Giesekus model. For each data set of fixed Ca, $\dot{\epsilon}$ is varied experimentally via H.

underestimation for Boger fluids [33]. The comparatively close agreement in Fig. 18 also confirms our argument that the polymer near the tip experiences large strain and steady-state stretching. Finally, the measured $\bar{\eta}$ increases with $\dot{\epsilon}$ as does the theoretical curve, albeit at a greater slope. This trend is consistent with prior measurements of Boger fluids, e.g. using opposed nozzles [20, 35] and contraction flows [33], although the absolute values are not comparable.

Figure 19 shows the FiSER measurements of $\bar{\eta}^+$ for the polymer solution used in our experiment. Apparently no steady stretching is approached in these tests. This is similar to CaBER measurements. In fact, the FiSER data agree fairly closely with the CaBER data reported in [32]. Besides, FiSER is limited to much higher strain rates than the selective withdrawal device. For these reasons, it is not a pertinent benchmark for the selective withdrawal device. The only connection we could make between FiSER and selective withdrawal measurements is a rather tenuous one. If we extrapolate the selective withdrawal data of Figs. 18 following the power-law trend to $\dot{\epsilon} = 3$ or 9 s^{-1}, we get $\bar{\eta}$ values on the order of 10^4 Pa·s, close to the maximum transient elongational viscosity attained in the FiSER data (Fig. 19). Of course, this should not be construed as a validation. The fact remains that there does not exist a good benchmarking device capable of doing similar measurements as the selective withdrawal device.
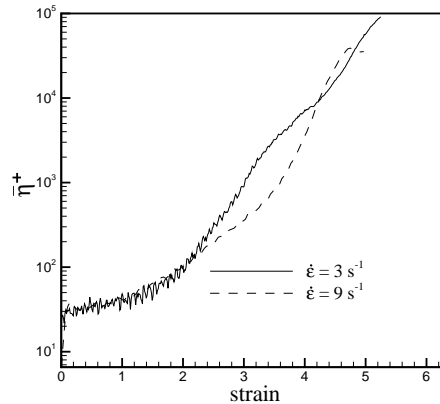
Figure 19: The transient elongational stress growth viscosity $\bar{\eta}^+$ of our experimental fluid measured at 27°C by filament stretching at two extension rates $\dot{\epsilon} = 3$ s^{-1} and 9 s^{-1} [34].

6   Conclusion

This paper presents numerical simulations of selective withdrawal to complement the experimental work in the accompanying paper [2]. There are two main results from this effort:

(a) We have elucidated the effects of viscoelasticity on interfacial deformation during selective withdrawal, including the depth of the depression and the tip curvature in the subcritical regime and the critical condition for jet formation.

(b) We have demonstrated the possibility of using selective withdrawal to measure the steady-state elongational viscosity of polymer solutions.

Regarding (a), the numerical computations show the correct trend in terms of increased deformation due to elastic stresses, and identified strain-hardening as the key mechanism at work. The limitations to this part of the results are the failures to reach the higher Deborah numbers in the experiment and to simulate the interfacial rupture. The former is a long-standing problem for viscoelastic computations, and newer schemes such as the logarithmic formalism offer hope of approaching higher Deborah numbers [36]. The latter problem is intrinsic to the sharp-interface formulation of the ALE method, and can only be remedied by alternative formulation of the interface, e.g., via diffuse-interface models [37, 38].

Regarding (b), we have examined the factors key to the success of this strategy, including the local flow type and the normal stress and strain rate at the tip, and compared the accuracy of the measurement with existing methods of extensional rheometry. Based on these, we have reached the preliminary conclusion that selective withdrawal can potentially be used as an extensional rheometer. Its maximum error of 47% for Newtonian fluids is superior to opposed-nozzle devices [20]. For polymer solutions, no definitive benchmark exists. But an estimated maximum error of about 300% compares favorably with opposed-nozzle and contraction flow devices [33, 35].

As an extensional rheometer, the selective withdrawal device has several unique advantages. Because the elongational stress and strain rate are sampled within a very small region surrounding the stagnation point, the procedure measures a *steady-stretching* elongational viscosity. None of the existing devices can access steady stretching readily. Moreover, thanks to its transducer-free scheme for determining the elongational stress, selective withdrawal can test low-viscosity liquids, and access much lower strain rates than other devices. Finally, the device is relatively immune to complicating factors such as inertia, spatial inhomogeneity and filament sagging common to other devices [11, 20].

We must note that our work on (b) suffers from two limitations. First, we have no direct measurement of the local strain rate at the tip. Consequently, we have to resort to numerical data to develop a correlation for the tip strain rate. This should be remedied in the future by direct PIV measurements of the local flow field [39], which may confirm and refine the correlation, and generalize it to wider parameter ranges. Second, there are no definitive benchmarks for polymer solutions to firmly establish the accuracy of the selective withdrawal protocol. Indeed, this is owing to the lack of a device capable of similar measurements, and speaks indirectly to the value of such a rheometer. Further investigation should aim to remove these uncertainties and optimize the design of the device.

References

[1] I. Cohen, S. R. Nagel, Scaling at the selective withdrawal transition through a tube suspended above the fluid surface, Phys. Rev. Lett. 88 (2002) 074501.

[2] D. Zhou, J. J. Feng, Selective withdrawal of polymer solutions: experiments, J. Non-Newtonian Fluid Mech. 165 (2010), 829–838.

[3] C. W. Macosko, Rheology: Principles, Measurements, and Applications, VCH Publishers, Inc., 1994.

[4] T. Sridhar, An overview of the project M1, J. Non-Newtonian Fluid Mech. 35 (1990) 85–92.

[5] D. F. James, K. A. Walters, A critical appraisal of available methods for the measurement of extensional properties of mobile systems, In A. A. Collyer, editor, Techniques in Rheological Measurement, Chapter 2, pages 33–53. Chapman & Hall, London, 1993.

[6] C. J. S. Petrie, Extensional viscosity: A critical discussion, J. Non-Newtonian Fluid Mech. 137 (2006) 15–23.

[7] S. L. Anna, G. H. McKinley, D. A. Nguyen, T. Sridhar, S. J. Muller, J. Huang, D. F. James, An interlaboratory comparison of measurements from filament-stretching rheometers using common test fluids, J. Rheol. 45 (2001) 83–114.

[8] G. H. McKinley, T. Sridhar, Filament-stretching rheometry of complex fluids, Ann. Rev. Fluid Mech. 34 (2002) 375–415.

[9] S. H. Spiegelberg, D. C. Ables, G. H. McKinley, The role of end-effects on measurements of extensional viscosity in fliament stretching rheometers, J. Non-Newtonian Fluid Mech. 64 (1996) 229–267.

[10] A. V. Bazilevsky, V. M. Entov, A. N. Rozhkov, Liquid filament microrheometer and some of its applications, In D. R. Oliver, editor, Third European Rheology Conference, pages 41–43. Elsevier, London, 1990.

[11] G. H. McKinley, A. Tripathi, How to extract the Newtonian viscosity from capillary breakup measurements in a filament rheometer, J. Rheol. 44 (2000) 653–670.

[12] G. H. McKinley, Visco-elastic-capillary thinning and break-up of complex fluids, In D. M. Bindings, K. Walters, editors, Rheology Reviews 2005, pages 1–49. The British Society of Rheology, 2005.

[13] K. S. Sujatha, H. Matallah, M. J. Banaai, M. F. Webster, Modeling step-strain filament-stretching (CaBER-type) using ALE techniques, J. Non-Newtonian Fluid Mech. 148 (2008) 109–121.

[14] C. Clasen, J. P. Plog, W. M. Kulicke, M. Owens, C. Macosko, L. E. Scriven, M. Verani, G. H. McKinley, How dilute are dilute solutions in extensional flows?, J. Rheol. 50 (2006) 849–881.

[15] M. R. Duxenneuner, P. Fischer, E. J. Windhab, J. J. Cooper-White, Extensional properties of hydroxypropyl ether guar gum solutions, Biomacromolecules 9 (2008) 2989–2996.

[16] E. Miller, C. Clasen, J. P. Rothstein, The effect of step-stretch parameters on capillary breakup extensional rheology (CaBER) measurements, Rheol. Acta 48 (2009) 625–639.

[17] T. R. Tuladhar, M. R. Mackley, Filament stretching rheometry and break-up behaviour of low viscosity polymer solutions and inkjet fluids, J. Non-Newtonian Fluid Mech. 148 (2008) 97–108.

[18] R. B. Bird, R. C. Armstrong, O. Hassager, Dynamics of Polymeric Liquids, Vol. 1. Fluid Mechanics, Wiley, New York, 1987.

[19] G. G. Fuller, C. A. Cathey, B. Hubbard, B. E. Zebrowski, Extensional viscosity measurements for low-viscosity fluids, J. Rheol. 31 (1987) 235–249.

[20] P. Dontula, M. Pasquali, L. E. Scriven, C. W. Macosko, Can extensional viscosity be measured with opposed-nozzle devices?, Rheol. Acta 36 (1997) 429–448.

[21] M. Pasquali, S. L. Scriven, Extensional flows and extensional rheometry, In A. Aït-Kadi, J. M. Dealy, D. F. James, M. C. Williams, editors, Proceedings of the XIIth International Congress on Rheology, pages 727–728, 1996.

[22] C. A. Cathey, G. G. Fuller, The optical and mechanical response of flexible polymer-solutions to extensional flow, J. Non-Newtonian Fluid Mech. 34(1) (1990) 63–88.

[23] J. C. Cai, P. R. de Souza Mendes, C. W. Macosko, L. E. Scriven, R. B. Secor, A comparison of extensional rheometers, In P. Moldenaers, R. Keunings, editors, Theoretical and Applied Rheology: Proceedings of the XIth International Congress on Rheology, Vol. 2, page 1012. Elsevier, Amsterdam, 1992.

[24] C. G. Hermansky, D. V. Boger, Opposing-jet viscometry of fluids with viscosity approaching that of water, J. Non-Newtonian Fluid Mech. 56 (1995) 1–14.

[25] P. Yue, J. J. Feng, C. A. Bertelo, H. H. Hu, An arbitrary Lagrangian-Eulerian method for simulating bubble growth in polymer foaming, J. Comput. Phys. 226 (2007) 2229–2249.

[26] H. H. Hu, Direct simulation of flows of solid-liquid mixtures, Int. J. Multiphase Flow 22 (1996) 335–352.

[27] H. H. Hu, N. A. Patankar, M. Y. Zhu, Direct numerical simulations of fluid-solid systems using the arbitrary Lagrangian-Eulerian technique, J. Comput. Phys. 169 (2001) 427–462.

[28] S. Courrech du Pont, J. Eggers, Sink flow deforms the interface between a viscous liquid and air into a tip singularity, Phys. Rev. Lett. 96 (2006) 034501.

[29] J. Eggers, S. Courrech du Pont, Numerical analysis of tips in viscous flow, Phys. Rev. E 79 (2009) 066311.

[30] P. Singh, L. G. Leal, Computational studies of the FENE dumbbell model in a co-rotating two-roll mill, J. Rheol. 38 (1994) 485–517.

[31] G. Astarita, Objective and generally applicable criteria for flow classification, J. Non-Newtonian Fluid Mech. 6 (1979) 69–76.

[32] D. Zhou, Interfacial Dynamics in Complex Fluids: Studies of Drop and Free-Surface Deformation in Polymer Solutions, PhD thesis, University of British Columbia, 2009.

[33] D. M. Binding, K. Walters, On the use of flow through a contraction in estimating the extensional viscosity of mobile polymer-solutions, J. Non-Newtonian Fluid Mech. 30 (1988) 233–250.

[34] D. F. James, M. Ouchi, Private communications, 2009.

[35] T. Schweizer, K. Mikkelsen, C. Cathey, G. Fuller, Mechanical and optical responses of the M1 fluid subject to stagnation point flow, J. Non-Newtonian Fluid Mech. 35 (1990) 277–286.

[36] M. A. Hulsen, R. Fattal, R. Kupferman, Flow of viscoelastic fluids past a cylinder at high Weissenberg number: Stabilized simulations using matrix logarithms, J. Non-Newtonian Fluid Mech. 127 (2005) 27–39.

[37] P. Yue, C. Zhou, J. J. Feng, C. F. Ollivier-Gooch, H. H. Hu, Phase-field simulations of interfacial dynamics in viscoelastic fluids using finite elements with adaptive meshing, J. Comput. Phys. 219 (2006) 47–67.

[38] P. Yue, C. Zhou, J. J. Feng, A computational study of the coalescence between a drop and an interface in Newtonian and viscoelastic fluids, Phys. Fluids 18 (2006) 102102.

[39] J. R. Herrera-Velarde, R. Zenit, D. Chehata, B. Mena, The flow of non-Newtonian fluids around bubbles and its connection to the jump discontinuity, J. Non-Newtonian Fluid Mech. 111 (2003) 199–209.